

Weak and reversed magnetic shear effects on internal kink and fishbone modes

Weikang Cai

State Key Laboratory of Advanced Electromagnetic Technology,
International Joint Research Laboratory of Magnetic Confinement Fusion and
Plasma Physics, School of Physics,
Huazhong University of Science and Technology, Wuhan, Hubei, 430074, China

Ping Zhu*

State Key Laboratory of Advanced Electromagnetic Technology,
International Joint Research Laboratory of Magnetic Confinement Fusion and
Plasma Physics, School of Electrical and Electronic Engineering,
Huazhong University of Science and Technology, Wuhan, Hubei, 430074, China;
Department of Nuclear Engineering and Engineering Physics,
University of Wisconsin-Madison, Madison, Wisconsin, 53706, United States of
America

E-mail: zhup@hust.edu.cn

Zhi Zhang

State Key Laboratory of Advanced Electromagnetic Technology,
International Joint Research Laboratory of Magnetic Confinement Fusion and
Plasma Physics, School of Physics,
Huazhong University of Science and Technology, Wuhan, Hubei, 430074, China

Shiwei Xue

State Key Laboratory of Advanced Electromagnetic Technology,
International Joint Research Laboratory of Magnetic Confinement Fusion and
Plasma Physics, School of Electrical and Electronic Engineering,
Huazhong University of Science and Technology, Wuhan, Hubei, 430074, China

Sui Wan

State Key Laboratory of Advanced Electromagnetic Technology,
International Joint Research Laboratory of Magnetic Confinement Fusion and
Plasma Physics, School of Electrical and Electronic Engineering,
Huazhong University of Science and Technology, Wuhan, Hubei, 430074, China

February 7th, 2026

Abstract.

Advanced tokamak scenarios often feature weak or reversed magnetic shear configurations. In this study, the hybrid kinetic-MHD model implemented in the NIMROD code is used to investigate the effects of reversed magnetic shear on internal kink and fishbone mode in a circular shaped limiter tokamak. In absence of energetic particles (EPs), the mode growth rate initially increases and then decreases as the magnetic shear changes from positive to negative, indicating stabilizing effects of the reversed magnetic shear on the internal kink mode. In presence of EPs, when the reversed magnetic shear region is sufficiently narrow, the transition from internal kink/fishbone modes to double kink/fishbone modes takes place, and the stabilizing effects of the reversed magnetic shear can significantly dominate the destabilization of EPs. For non-resonant modes, the EP beta fraction β_f for excitation increases with q_{\min} , concurrent with progressively lower growth rates in non-resonant fishbone modes. When the equilibrium profile has an internal transport barrier (ITB), broader ITB widths suppress internal kink modes more effectively, whereas steeper temperature gradients strengthen EP stabilization.

Keywords: internal kink mode, fishbone, reversed magnetic shear, energetic particles, double kink/fishbone modes, NIMROD

1. Introduction

The internal kink instability imposes constraints on the maximum plasma current density in the core region of a tokamak. The energetic particles (EPs) from auxiliary heating and fusion reactions can strongly interact with the internal kink mode [1, 2, 3] and excite the fishbone mode. Since the initial observation of fishbone modes on PDX [4] during high-power Neutral Beam Injection (NBI) in 1980s, these modes have been observed on other tokamaks, including DIII-D [5], JET [6], HL-2A [7], and EAST [8], among others, in presence of various forms of auxiliary heating, such as perpendicular/parallel NBI, Electron Cyclotron Resonant Heating (ECRH), or Ion Cyclotron Resonant Heating (ICRH). Theoretical studies indicate that fishbone modes are triggered by the resonant interaction between the trapped EPs and the internal kink modes, as well as the diamagnetic dissipation from the background plasmas [9, 10] or the resonance between the circulating EPs and the internal kink modes, along with the effects of finite radial particle-orbit excursion [11, 12]. Based on EAST-like parameters, using the kinetic-MHD hybrid code M3D-K for simulations of the fishbone instabilities, Shen et al show that the dual resonant fishbone (DRF) is excited by the trapped beam ions when the fast ion pressure exceeds a critical value, and the mode structure of DRF exhibits splitting radial structure due to double $q = 1$ surfaces [13].

During the NBI heating of plasmas with flat central safety factor profile, long-lived modes (LLMs) are observed on HL-2A that can last for several hundred milliseconds, and the mode frequency is approximately proportional to the toroidal mode number n [14]. The LLMs can be suppressed by ECRH or SMBI (supersonic molecular beam injection)

which is related to changing of q profile and pressure gradient[14]. The excitation of fishbone modes in tokamak plasmas with positive magnetic shear depends on $q' = dq/dr$ at $q = 1$ surface[3, 15]. However, in the case of reversed magnetic shear regimes, conventional fishbone analysis may not be sufficient to explain the fast ion driven mode [16, 17]. When the safety factor profile q_0 is close to unity, the fast ion-driven mode can be observed even with a non-monotonic q -profile, as reported in experiments conducted on DIII-D [5], NSTX [18], and MAST [19]. The growth rate of the kink mode with the reversed magnetic shear given is also valid in $q_{\min} > 1$ and $q'_s = 0$ cases[20].

The impact of safety factor profile, particularly in presence of very weak magnetic shear, on the $m/n = 1$ mode triggered by energetic ions in tokamak plasmas has been investigated through numerical simulations and theoretical analysis [21, 22, 23, 24]. In presence of reversed magnetic shear, a double fishbone mode (DFM) can arise when $q_{\min} < 1$, whose mode structure is distinct from that of the conventional double kink mode. The frequency of DFM is found to be in close proximity to half of the average EP precession frequency [22]. Solving an analytical dispersion relation developed for non-resonant fishbone (NRF) with reversed magnetic shear configuration, Wang et al find that the growth rate with $q_{\min} > 1$ depends on the fast ion beta β_h in a power law of $\sim \beta_h^{2/3}$, different from that of $\sim \beta_h$ in a conventional positive magnetic shear configuration [23]. Recent 3D resistive MHD simulations using the M3D-C1 code have also identified a dominant non-resonant $(1, 1)$ infernal mode in spherical tokamak plasmas when q_{\min} approaches unity from above ($q_{\min} \sim 1.1 - 1.2$), which can lead to a nonlinear flattening of the core current and pressure profiles [25]. Based on the equilibrium with flat q -profile in core plasma region generated from the LLM experiments on HL-2A, Zou et al show that the EP-driven fishbone mode frequency is almost proportional to the toroidal mode number n even in absence of any equilibrium toroidal flow, using the hybrid kinetic-MHD model implemented in the NIMROD code [24].

Despite this progress, a consistent understanding on the effects of reversed magnetic shear on internal kink and fishbone modes based on both theory and simulation remains desirable. In this study, we investigate the influence of continuously various q -profiles on the instability induced by energetic particles (EPs), using simulation based on the hybrid kinetic-MHD model implemented in the NIMROD code [26, 27, 28], and in the context of previous theoretical formulation. Both simulation and theory have been able to demonstrate the dominant stabilizing effects of the reversed magnetic shear over the destabilizing effects of EPs on internal kink mode.

The remainder of this paper is structured as follows. Section 2 provides a brief review of the simulation model. In section 3 we specify the simulation setup. In section 4, we report the main results about the effects of magnetic shear and EP β fraction on the kink/fishbone mode. Finally, in section 5, we summarize and discuss the findings.

2. Simulation model

This study is based on a set of hybrid kinetic-MHD equations implemented in the NIMROD code [26, 27]

$$\frac{\partial \rho}{\partial t} + \nabla \cdot (\rho \mathbf{V}) = 0, \quad (1)$$

$$\rho \left(\frac{\partial \mathbf{V}}{\partial t} + \mathbf{V} \cdot \nabla \mathbf{V} \right) = \mathbf{J} \times \mathbf{B} - \nabla p_b - \nabla \cdot P_h, \quad (2)$$

$$\frac{n}{\Gamma - 1} \left(\frac{\partial T}{\partial t} + \mathbf{V} \cdot \nabla T \right) = -p \nabla \cdot \mathbf{V} - \nabla \cdot \mathbf{q} + Q, \quad (3)$$

$$\frac{\partial \mathbf{B}}{\partial t} = -\nabla \times \mathbf{E}, \quad (4)$$

$$\nabla \times \mathbf{B} = \mu_0 \mathbf{J}, \quad (5)$$

$$\mathbf{E} = -\mathbf{V} \times \mathbf{B}, \quad (6)$$

where ρ , \mathbf{V} , \mathbf{J} , p_b , n and T are the mass density, center of mass velocity, current density, plasma pressure, number density, and temperature of the main species plasma, \mathbf{E} and \mathbf{B} are the electric and magnetic fields, Γ and μ_0 are the specific heat ratio and the vacuum permeability, respectively. \mathbf{q} and Q are the heat flux and the heating source terms, which are not considered for the modes we study here. By adding the pressure tensor of energetic particles to the momentum equation, which is defined as

$$P_h = m_h \int \Delta \mathbf{v}_h \Delta \mathbf{v}_h f_h d^3 \mathbf{v}_h, \quad (7)$$

the effects of energetic particles can be included, where $\Delta \mathbf{v}_h = \mathbf{v}_h - \mathbf{V}_h$, and m_h , \mathbf{v}_h , f_h , \mathbf{V}_h are the mass, velocity, distribution function, and the center of mass velocity of EPs, respectively.

3. Simulation setup

A circular-shaped tokamak equilibrium with the pressure profile $q(\psi) = a(\psi - c)^2 + b(\psi - c)(\psi - 1) + 1$ and the safety factor profile $p(\psi) = p_0(\psi^2 - 2\psi + 1)$ is generated using the CHEASE code, where ψ represents the normalized poloidal magnetic flux and a magnetic flux-aligned mesh is adopted (figure 1). The internal kink mode is located within a region $0 < \sqrt{\psi/\psi_0} < 0.6$ where the safety factor q -profile is below unity and the magnetic shear is weak [figure 1(b)]. Here, ψ denotes the poloidal magnetic flux and ψ_0 represents the total poloidal magnetic flux inside the last closed flux surface.

Initially the energetic particles are assumed to follow the slowing-down distribution [26],

$$f_0 = \frac{P_0 \exp \left(\frac{P_c}{\psi_n} \right)}{\varepsilon^{3/2} + \varepsilon_c^{3/2}}, \quad (8)$$

where P_0 is the normalization constant, $P_\zeta = g\rho_{\parallel} - \psi_p$ is the canonical toroidal momentum, $g = RB_\phi$, $\rho_{\parallel} = mv_{\parallel}/qB$, ψ_p is the poloidal flux, $\psi_n = c\psi_0$, ψ_0 is the total poloidal flux and the parameter c is used to match the spatial profile of the equilibrium, ε is the EP energy, and ε_c is the critical slowing-down energy [29]

$$\varepsilon_c = \left(\frac{3}{4}\right)^{2/3} \left(\frac{\pi m_i}{m_e}\right)^{1/3} T_e, \quad (9)$$

with m_i being the ion mass, m_e the electron mass, and T_e the electron temperature. In our linear simulation, we set resistivity $\eta = 0$, and a total 2×10^6 simulation particles are prescribed in the poloidal plane with 64×64 bicubic finite elements. The remaining parameters are set up as follows: major radius $R_0 = 1.0$ m, aspect ratio $R_0/a = 2.8$, magnetic axis $R_m = 1.06$ m, maximum toroidal magnetic $B_{\max} = 1.0$ T, and the number density is uniform in the radial direction with $n_e = 2.489 \times 10^{19} \text{ m}^{-3}$ [26].

4. Calculation results

4.1. Magnetic shear effects in absence of EPs

In figure 1(b), we vary the value of b for the same values of a and c , thereby altering the magnetic shear \hat{s} from -0.8 to 0.8, with the location of the $q = 1$ surface fixed at $\psi_s = 0.1$.

In absence of EPs, the (1, 1) internal mode growth rate first increases as the positive magnetic shear decreases to zero and becomes reversed, reaching a maximum value near $\hat{s} = -0.2$, and then starts to decrease as the magnetic shear reversal continues. Such shear effects may be understood from the previous analytical theory, where the growth rate of the mode in positive magnetic shear region can be expressed as [21]

$$\frac{\gamma}{\omega_A} = -\frac{1}{\sqrt{3}\hat{s}} \delta\widehat{W}_{\text{MHD}}, \quad (10)$$

where $\omega_A = V_A/qR_0 = V_A/R_0$ is the Alfvén frequency on the $q = 1$ surface, $\hat{s} = r_sq'/q$ is the magnetic shear at $q = 1$ surface, r_s is the radius of the $q = 1$ surface, and $\delta\widehat{W}_{\text{MHD}}$ can be written in the form of

$$\delta\widehat{W}_{\text{MHD}} \approx 3\pi\delta q\varepsilon_1^2 (\beta_{pc}^2 - \beta_p^2), \quad (11)$$

where the poloidal plasma beta

$$\beta_p = -\left(8\pi/B_0^2\right) \int_0^{r_s} (r/r_s)^2 (dp/dr) dr, \quad (12)$$

$\varepsilon_1 = r_s/R_0$, and $\delta q = 1 - q(r = 0) = 1 - q_0$. For flattened q -profiles with $q_0 < 1$ and a finite δq , one finds a threshold of plasma beta, i.e., $\beta_{pc} = \left[\frac{13(4-v)}{48(4+v)}\right]^{1/2}$, for a parabolic q -profile, $v = 2$. From Eq. (10), it can be seen that when the location of the resonant surface and the p -profile are fixed, as shown in figure 1(a), $\delta\widehat{W}_{\text{MHD}}$ is mainly affected by

δq , which indicates that the magnetic shear \hat{s} is stabilizing whereas δq is destabilizing on the mode. In positive magnetic shear region, it can be concluded that when $\hat{s} < 0.72$, the increase of magnetic shear plays a dominant role in enhancing the stabilizing effects on the mode. When $\hat{s} > 0.72$, the increase of δq dominates the enhanced destabilizing effects on the mode and increasing the growth rate, as shown in figure 2(a). Previously, only the case where the growth rate decreases with the increase of magnetic shear is reported [21]. This may be because the magnetic shear at the resonant surface is not large enough to reveal the destabilizing effects of δq on the mode.

In the weak reversed magnetic shear region, the mode growth rate first increases and then decreases with decreasing magnetic shear, reaching a maximum value near $\hat{s} = -0.2$. As shown in figure 2(b), the growth rate increases first and then decreases as q_{\min} increases, which is consistent with the analytical result in [21]

$$\bar{\gamma} [(\bar{\gamma} + \Delta q) r_{\min}^2 q'']^{1/2} = -\delta \widehat{W}_{\text{MHD}}, \quad (13)$$

where $\bar{\gamma} = [3\gamma^2/\omega_A^2 + (\Delta q)^2]^{1/2}$, $q_{\min} = q(r_{\min})$, $\Delta q = q_{\min} - 1$, $r_{\min}^2 q'' = r_{\min}^2 d^2 q/dr^2$ at $q = q(r_{\min})$ surface, and $\delta \widehat{W}_{\text{MHD}}$ is given in Eq. (11). In comparison with the q -profiles in [21], for a fixed resonance surface, in this study the change in the magnitude of $r_{\min}^2 q''$ near the $q = q_{\min}$ surface is not significant. Therefore, the reason for the growth rate variation with q_{\min} is mainly due to the variation in Δq . The growth rate of the $q_{\min} < 1$ profile rises with q_{\min} , as a result of the enhanced coupling between the two resonant surfaces as q_{\min} increases. When the q_{\min} surface approaches the $q = 1$ surface, the mode growth rate decreases, likely because the mode becomes less resonant.

The plasma pressure perturbation contour indicates that the mode structure contracts as \hat{s} increase (figure 3). For the positive magnetic shear, the mode structure is a single kink mode within the $q < 1$ region; for the reversed magnetic shear, the mode structure is that of a double kink mode between two $q = 1$ surfaces. The mode structures in figure 3(a) and (b) are highly consistent with those obtained using analytical methods in [22]. When the two resonant surfaces are relatively far apart, the double kink modes structure appears more prominent, with the first layer of modes located within the first resonant surface and the second layer of modes between the two resonant surfaces. As the two resonant surfaces draw closer together, the layered mode structure becomes less obvious.

4.2. Magnetic shear effects in presence of EPs

In presence of EPs, when β_f is low, e.g. $\beta_f = 0.1$, the growth rates are reduced, but the overall trend is similar to the case without EPs [figure 4(a)]. When β_f increases, e.g. $\beta_f = 0.5$, the growth rate increases relative to the case without EPs when $\hat{s} > -0.25$, which is attributed to the excitation of fishbone modes. In contrast, for $\hat{s} < -0.25$, the growth rate decreases, and increasing magnetic shear further reduces the growth rate, demonstrating its stabilizing effect [21].

In the case where the magnetic shear is between -0.2 and 0.2 (figure 5), we observe that the mode growth rate and real frequency exhibit a similar trend. Specifically, the growth rate decreases initially, and then increases with an increase in β_f , whereas the real frequency increases with β_f . For the case with $\hat{s} = -0.6, -0.8$ (figure 6), it is observed that the presence of energetic particles can lead to a reduction in the growth rate of the mode, indicating stabilizing effects. The growth rate of the mode can be expressed as [22]

$$\frac{\gamma}{\omega_A} = \frac{\left| \operatorname{Re} \left(\delta \widehat{W}_K \right) \right|}{\sqrt{3} \left[(1 - M)^2 \hat{s}_1 + M^2 (r_2/r_1)^2 \hat{s}_2 \right]}, \quad (14)$$

where $\delta \widehat{W}_K$ is the kinetic energy of trapped fast particles, r_1 and r_2 are the positions of the two resonant surfaces, M denotes the ratio of displacement amplitudes at the inner and outer $q = 1$ resonant surfaces, and \hat{s}_1 and \hat{s}_2 are the magnetic shears of the two resonant surfaces. When \hat{s}_1 is sufficiently negative, $(1 - M)^2 \hat{s}_1 + M^2 (r_2/r_1)^2 \hat{s}_2 < 0$, which leads to a stronger stabilizing effects on the mode when the energetic particles fraction increases.

Additionally, the real frequency of the mode still shows a monotonic increase with increasing β_f , even for $\hat{s} = -0.6$. However, for the case with $\hat{s} = -0.8$, the real frequency no longer shows a monotonic increase with increasing β_f . The plasma pressure perturbation contours (figure 7) indicate that the mode structure transitions from a double kink mode to a double fishbone mode as β_f increases.

4.3. Non-resonant modes in presence of EPs

The growth rate of the non-resonant mode when $q_{\min} > 1$ can be expressed as [30]

$$\gamma/\omega_A = \frac{1}{\sqrt{3}S^{2/3}} \operatorname{Re} \left[\left(-\delta \widehat{W}_{\text{MHD}} - \delta \widehat{W}_K \right)^{2/3} \right] - \Delta q / 3\sqrt{3}, \quad (15)$$

where $S = \sqrt{r_s^2 q_s''}$, $\Delta q = q_{\min} - 1$. Equation (15) demonstrates that Δq stabilizes the mode, whereas β_f destabilizes it. When Δq decreases below 0.02, the term $\Delta q / 3\sqrt{3}$ becomes negligible. The mode growth rate consequently reduces to that of the resonant fishbone mode derived in [21]. Increasing Δq raises the critical β_f required for non-resonant mode excitation and simultaneously lowers the growth rate.

The above theory prediction on the non-resonant mode is verified in our simulations. Given that the typical experimental uncertainty of the safety factor profile is approximately 5% \sim 10% [31, 32], simulations are performed with q_{\min} varying from 1.01 to 1.20. For $q_{\min} \geq 1$, the growth rate of non-resonant internal kink exhibits similarities to the resonant modes (figure 8(b)). Increasing β_f drives a transition from the internal kink to the fishbone mode. Resonant internal kink modes are absent for $q_{\min} > 1.02$. Above critical β_f thresholds, only non-resonant fishbone modes emerge, with growth rates decreasing as q_{\min} rises, in agreement with the Δq stabilization indicated in Eq.(15). A similar dependency on the safety factor profile is also found

in resistive MHD simulations, where a dominant non-resonant (1, 1) infernal mode is excited as q_{\min} decreases towards unity, further confirming the destabilizing effect of reducing Δq [25].

4.4. Effects due to internal transport barrier profile

To examine the effects from an internal transport barrier (ITB), the following equilibrium temperature profile is adopted

$$T = A \frac{(1 + \alpha z)e^z - (1 - \beta z)e^{-z}}{e^z + e^{-z}} + T_0, \quad (16)$$

where $z = (\rho_{\text{ITB}} - \rho)/w_{\text{ITB}}$, ρ is the normalized radial coordinate, ρ_{ITB} is the ITB location, and w_{ITB} is the ITB width. A , α , β , and T_0 are additional profile shaping coefficients. In the simulations, we selected $\rho_{\text{ITB}} = 0.35$, $w_{\text{ITB}} = 0.14$, $A = 0.45$, $\alpha = 0.06$, $\beta = 0.3$, and $T_0 = 1.45$ (figure 9).

Varying the magnetic shear \hat{s} from -0.8 to 0.8, the variation of mode growth rate with magnetic shear remains similar to the case in absence of an ITB (Figure 10). For the q profile with reversed magnetic shear ($\hat{s} = -0.6$), the growth rate of the internal kink mode decreases as the ITB becomes wider. As the ITB becomes steeper (figure 11), the stabilizing effect of energetic particles become more pronounced (figure 12). This finding agrees with the numerical simulation results reported by Ge et al [33].

5. Conclusions and discussions

Kinetic-MHD simulations using the NIMROD code are performed to investigate the impact of weak and reversed magnetic shear on the internal kink mode in tokamaks. For the resonant (1,1) mode, its growth rate increases as the magnetic shear at $q = 1$ surface reduces from positive to zero and negative, until the growth rate reaches its maximum value at a finite negative magnetic shear. Further increasing the absolute value of the negative magnetic shear at $q = 1$ surface starts to stabilize the (1,1) mode with reduced growth rate. Such effects of weak and reversed magnetic shear on the (1,1) kink mode persist in presence of EPs. For non-resonant modes with q_{\min} slightly above 1, i.e. $\Delta q = q_{\min} - 1 \lesssim 0.02$, the dynamics closely resemble those of resonant modes. When q_{\min} rises sufficiently above 1, i.e. $\Delta q \gtrsim 0.02$, the critical β_f required to trigger non-resonant modes grows proportionally to Δq , and the growth rate decreases with Δq . These results agree quantitatively with previous theoretical calculations [21].

Future work plans on exploring the effects of the weak and reversed magnetic shear on the nonlinear internal kink and fishbone mode during sawtooth and ITB formation processes in the advanced tokamak configurations.

Acknowledgements

We are grateful to Prof. Xianqu Wang and Dr. Haolong Li, as well as the support of the NIMROD team. This work is supported by the National MCF Energy R&D Program of China under Grant No. 2019YFE03050004, the Hubei International Science and Technology Cooperation Project under Grant No. 2022EHB003, and the U.S. Department of Energy Grant No. DE-FG02-86ER53218. The computing work in this paper is supported by the Public Service Platform of High Performance Computing by Network and Computing Center of HUST.

References

- [1] Shafranov V D 1970 *Soviet Physics Technical Physics* **15** 175
- [2] Rosenbluth M N, Dagazian R Y and Rutherford P H 1973 *The Physics of Fluids* **16** 1894–1902
- [3] Bussac M N, Pellat R, Edery D and Soule J L 1975 *Physical Review Letters* **35** 1638
- [4] McGuire K, Goldston R, Bell M *et al.* 1983 *Physical Review Letters* **50** 891
- [5] Wong K L, Chu M S, Luce T C *et al.* 2000 *Physical Review Letters* **85** 996
- [6] Nave M F F, Campbell D J, Joffrin E *et al.* 1991 *Nuclear Fusion* **31** 697
- [7] Chen W, Ding X T, Liu Y *et al.* 2010 *Nuclear Fusion* **50** 084008
- [8] Xu L Q, Zhang J Z, Chen K Y *et al.* 2015 *Physics of Plasmas* **22**
- [9] Chen L, White R B and Rosenbluth M N 1984 *Physical Review Letters* **52** 1122
- [10] Coppi B and Porcelli F 1986 *Physical Review Letters* **57** 2272
- [11] Betti R and Freidberg J P 1993 *Physical Review Letters* **70** 3428
- [12] Wang S J 2001 *Physical Review Letters* **86** 5286
- [13] Shen W, Wang F, Fu G Y, Xu L Q and Ren Z Z 2020 *Nuclear Fusion* **60** 106016
- [14] Wei D, Yi L, Wang X Q *et al.* 2013 *Nuclear Fusion* **54** 013010
- [15] Hu B, Betti R and Manickam J 2006 *Physics of Plasmas* **13**
- [16] Zonca F, Buratti P, Cardinali A *et al.* 2007 *Nuclear Fusion* **47** 1588
- [17] Zonca F and Chen L 2014 *Physics of Plasmas* **21**
- [18] Wang F, Fu G Y, Breslau J A *et al.* 2013 *Physics of Plasmas* **20**
- [19] Chapman I T, Hua M D, Pinches S D *et al.* 2010 *Nuclear Fusion* **50** 045007
- [20] Hastie R J, Hender T C, Carreras B A *et al.* 1987 *The Physics of Fluids* **30** 1756–1766
- [21] Li Z Y, Wang X Q and Wang X G 2015 *Chinese Physics B* **25** 015203
- [22] Meng G, Wang X Q, Wang X G *et al.* 2015 *Physics of Plasmas* **22**
- [23] Wang X Q and Wang X G 2015 *Plasma Physics and Controlled Fusion* **57** 025019
- [24] Zou Z H, Zhu P, Kim C C *et al.* 2022 *Plasma Science and Technology* **24** 124005
- [25] Jardin S 2025 *Physics of Plasmas* **32** 082503
- [26] Kim C C *et al.* 2008 *Physics of Plasmas* **15** 072507
- [27] Sovinec C R, Glasser A H, Gianakon T A *et al.* 2004 *Journal of Computational Physics* **195** 355–386
- [28] Brennan D P, Kim C C and La Haye R J 2012 *Nuclear Fusion* **52** 033004
- [29] Goldston R and Rutherford P 1995 *Introduction to Plasma Physics* (CRC Press)
- [30] Wang X Q, Zhang R B, Qin L and Wang X G 2014 *Plasma Physics and Controlled Fusion* **56** 095013
- [31] Soltwisch H 1986 *Review of Scientific Instruments* **57** 1939–1944
- [32] Levinton F M, Batha S H, Yamada M and Zarnstorff M C 1993 *Physics of Fluids B: Plasma Physics* **5** 2554–2561
- [33] Ge W, Wang Z X, Wang F, Liu Z and Xu L 2022 *Nuclear Fusion* **63** 016007

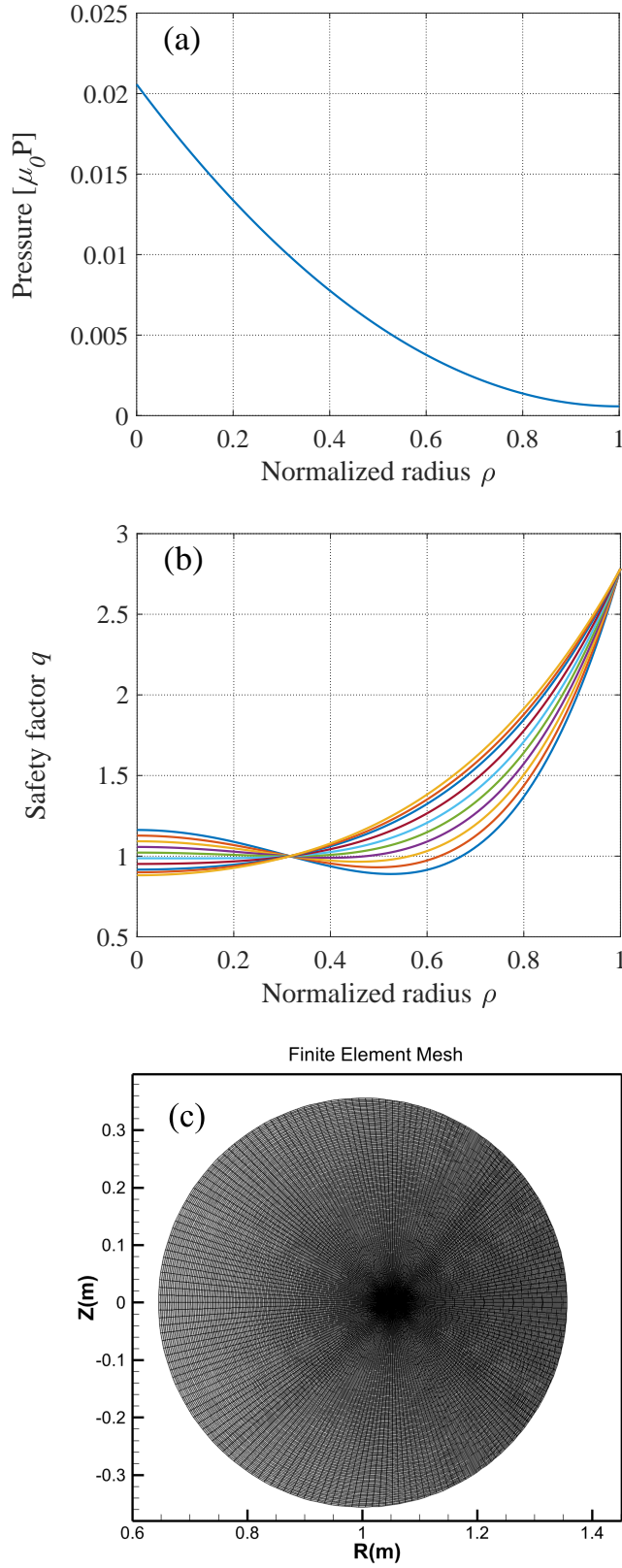


Figure 1. (a) Equilibrium pressure profile and (b) q -profiles as functions of normalized minor radius ρ with various magnetic shear \hat{s} at $q = 1$ surface. (c) Equilibrium magnetic flux-aligned mesh for poloidal plane used in NIMROD simulations.

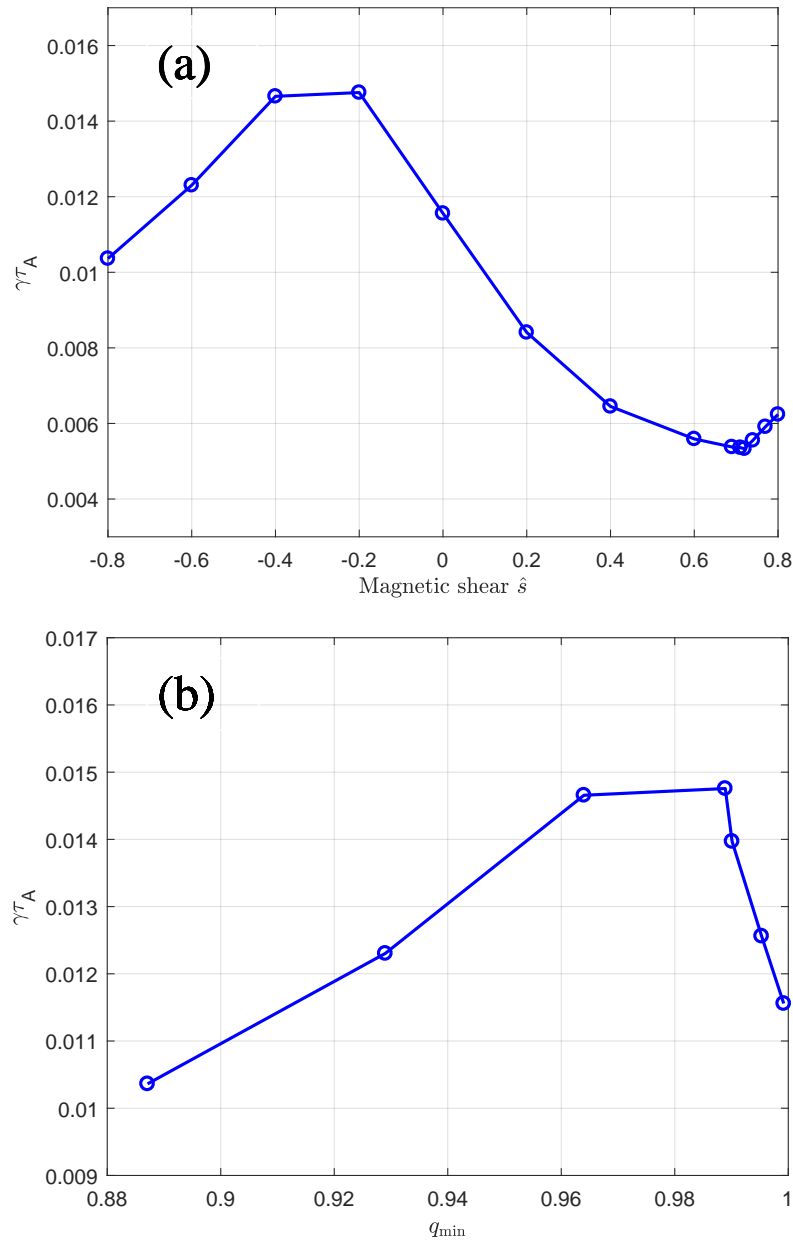


Figure 2. Normalized growth rates of the $(m, n)=(1, 1)$ mode as functions (a) the magnetic shear \hat{s} at $q = 1$ surface and (b) the minimum of q profile q_{\min} in absence of EPs.

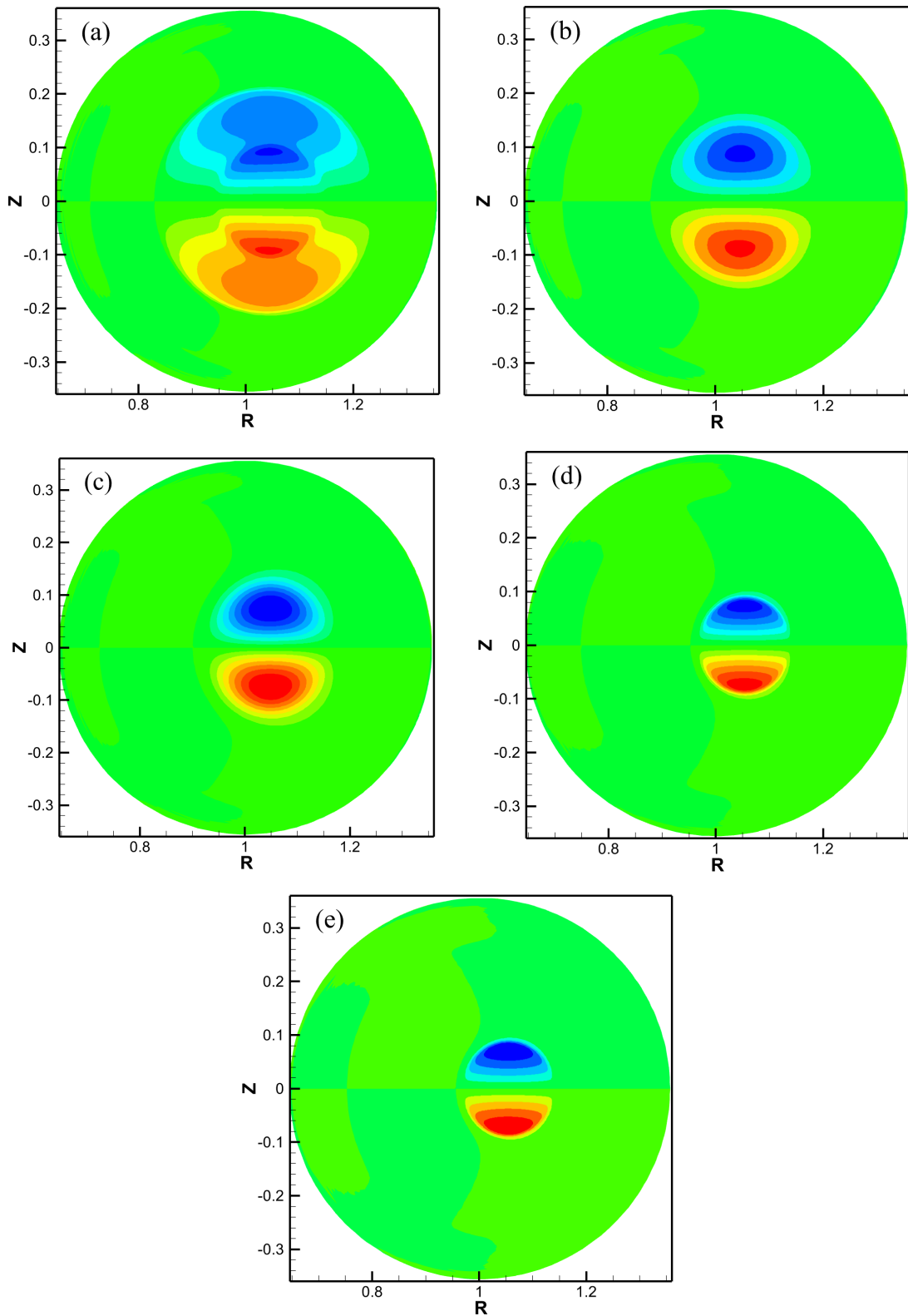


Figure 3. Pressure perturbation contours of the 1/1 kink mode in absence of EPs for the magnetic shear (a) $\hat{s} = -0.8$, (b) $\hat{s} = -0.2$, (c) $\hat{s} = 0$, (d) $\hat{s} = 0.7$, (e) $\hat{s} = 0.8$ at $q = 1$ surface.

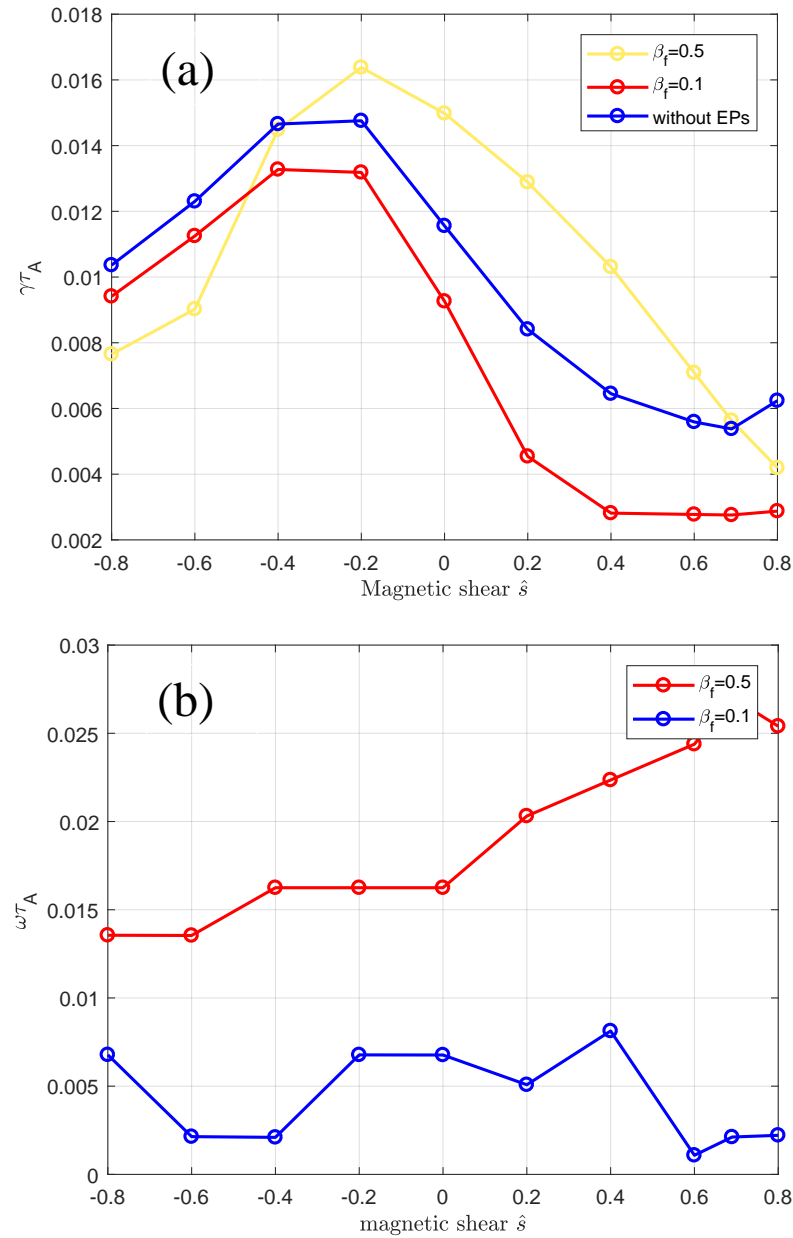


Figure 4. (a) Normalized growth rates and (b) real frequencies as functions of the magnetic shear \hat{s} at $q = 1$ surface for $\beta_f = 0.1, 0.5$.

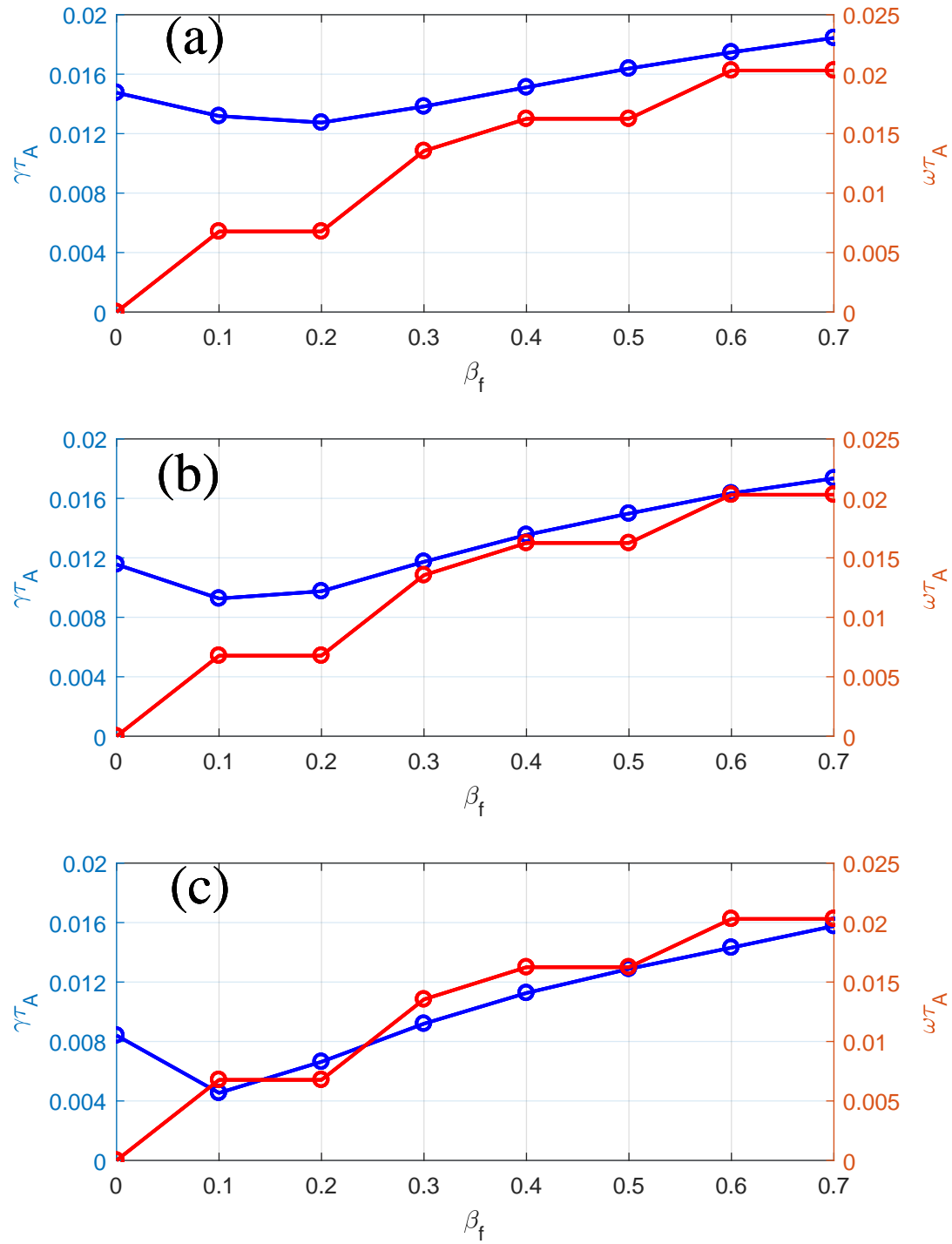


Figure 5. Normalized growth rates and real frequencies as functions of the EP beta fraction β_f for (a) $\hat{s} = -0.2$, (b) $\hat{s} = 0$, (c) $\hat{s} = 0.2$ at $q = 1$ surface.

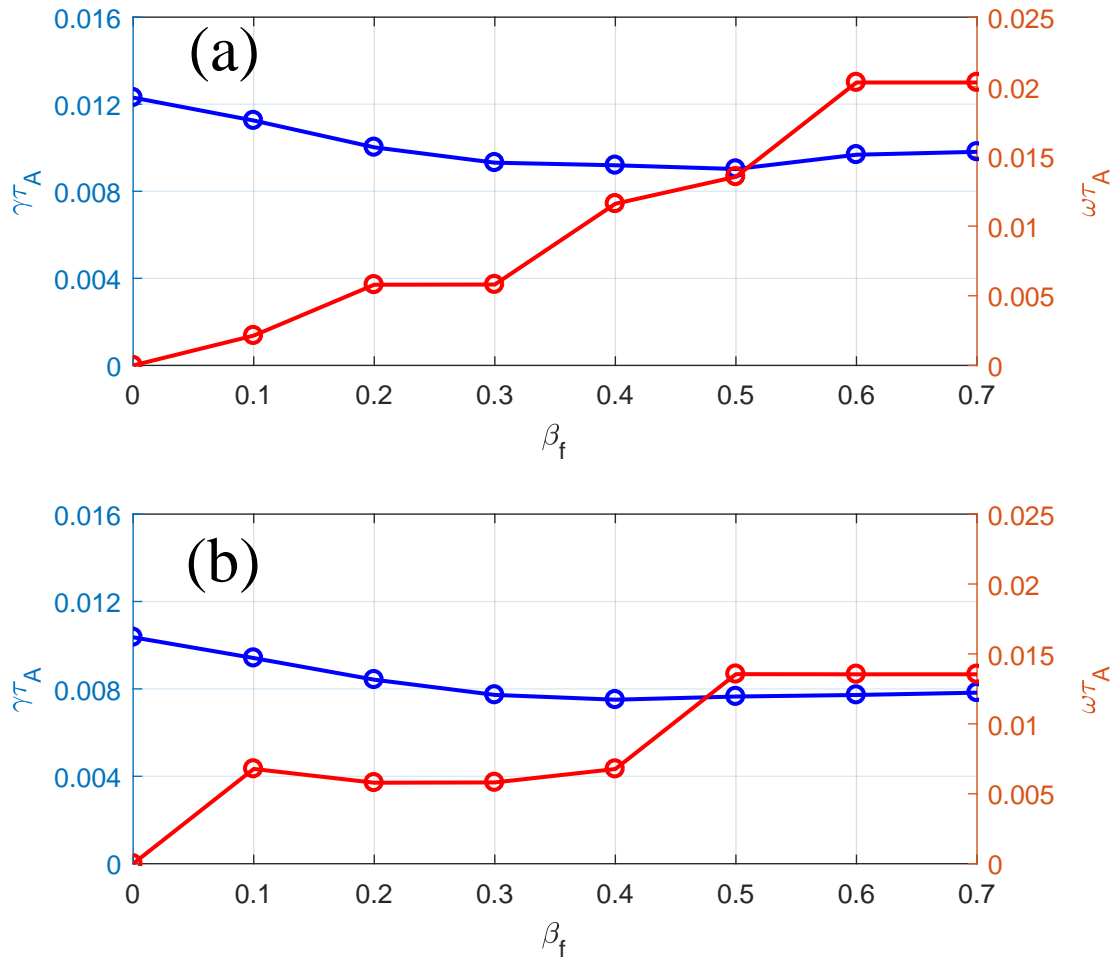


Figure 6. Normalized growth rates and real frequencies as functions of the EP beta fraction β_f for (a) $\hat{s} = -0.6$, (b) $\hat{s} = -0.8$ at $q = 1$ surface.

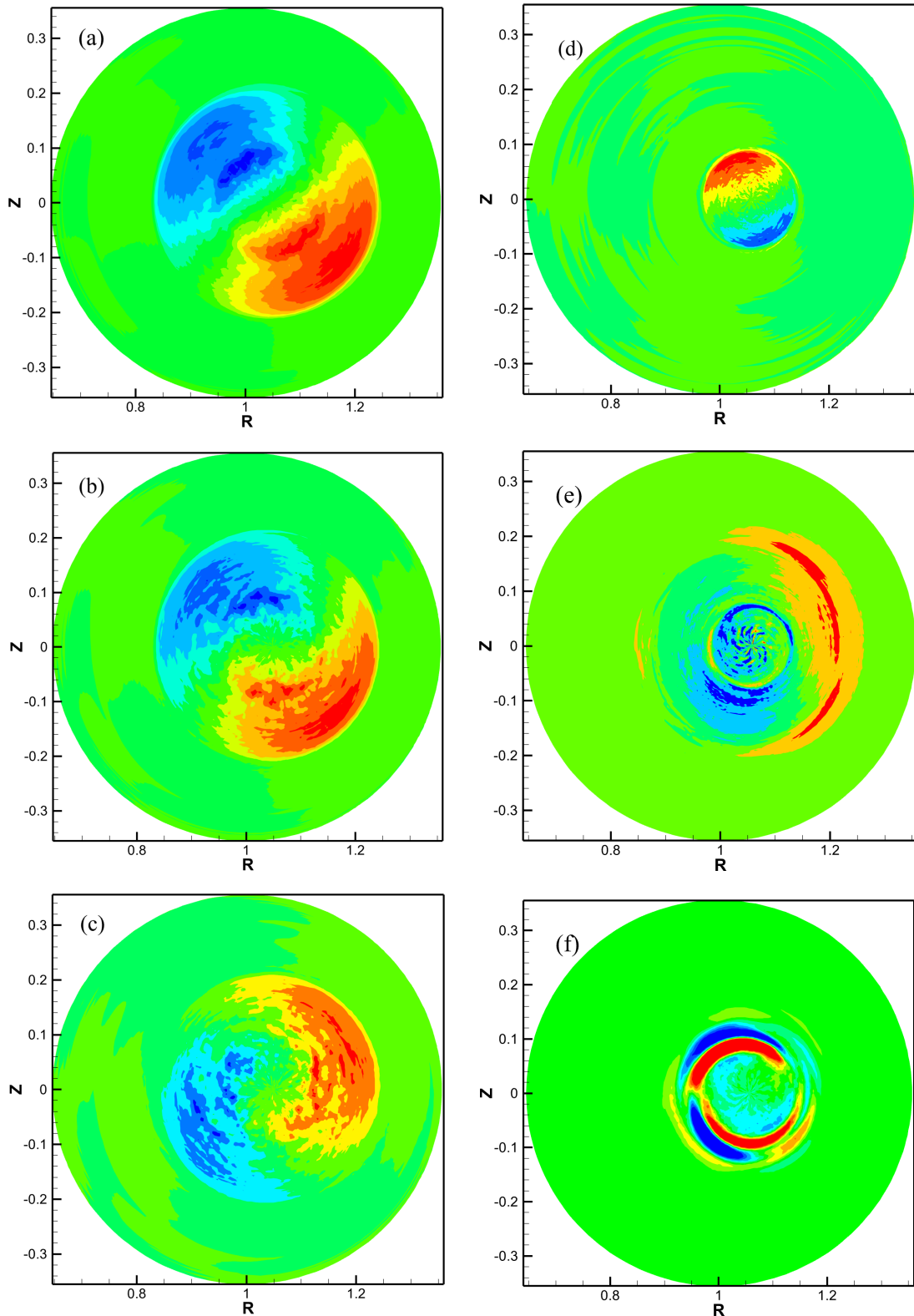


Figure 7. Pressure perturbation contours of the 1/1 kink mode for (a-c) $\hat{s} = -0.8$ and (d-f) $\hat{s} = 0.8$ at $q = 1$ surface with various EP- β fractions: [(a) and (d)] $\beta_f = 0.2$, [(b) and (e)] $\beta_f = 0.4$, and [(c) and (f)] $\beta_f = 0.6$.

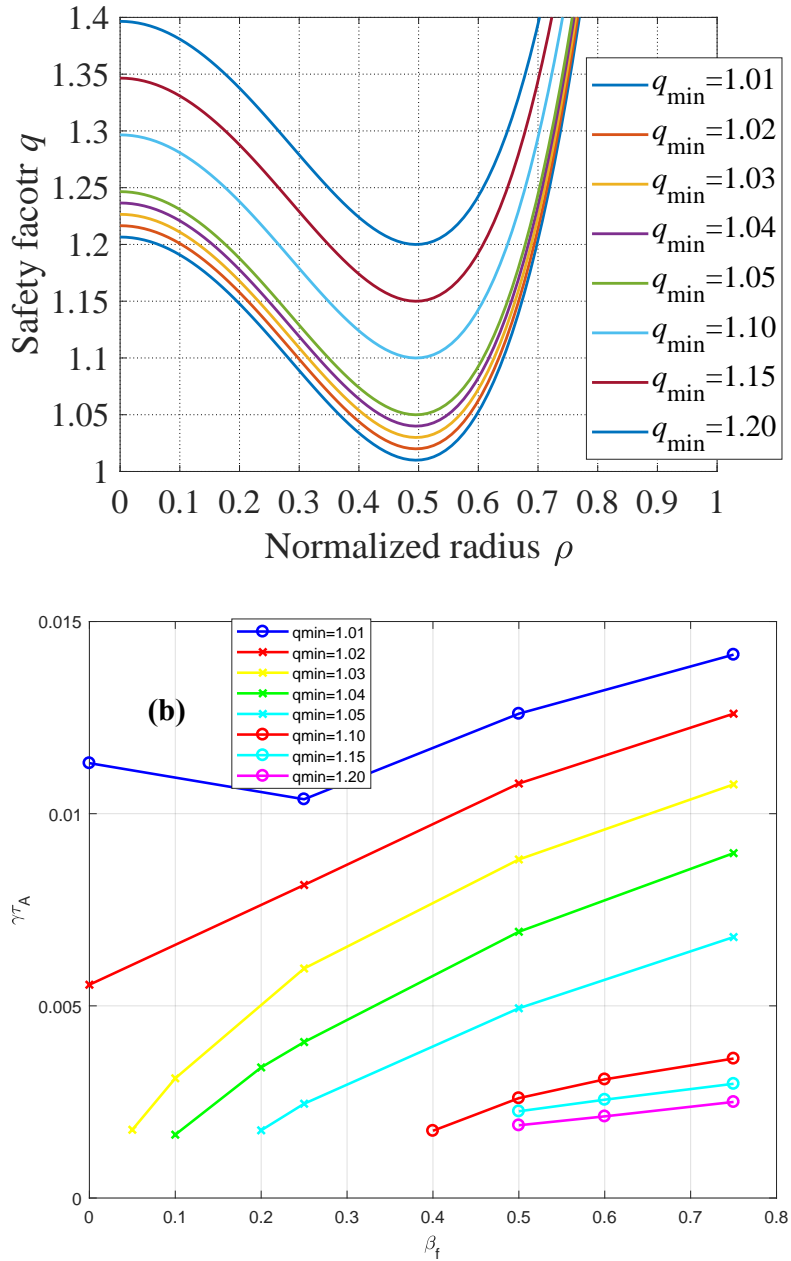


Figure 8. Non-resonant q profiles with various q_{\min} and (b) normalized growth rates of the non-resonant modes as functions of β_f for various q_{\min} .

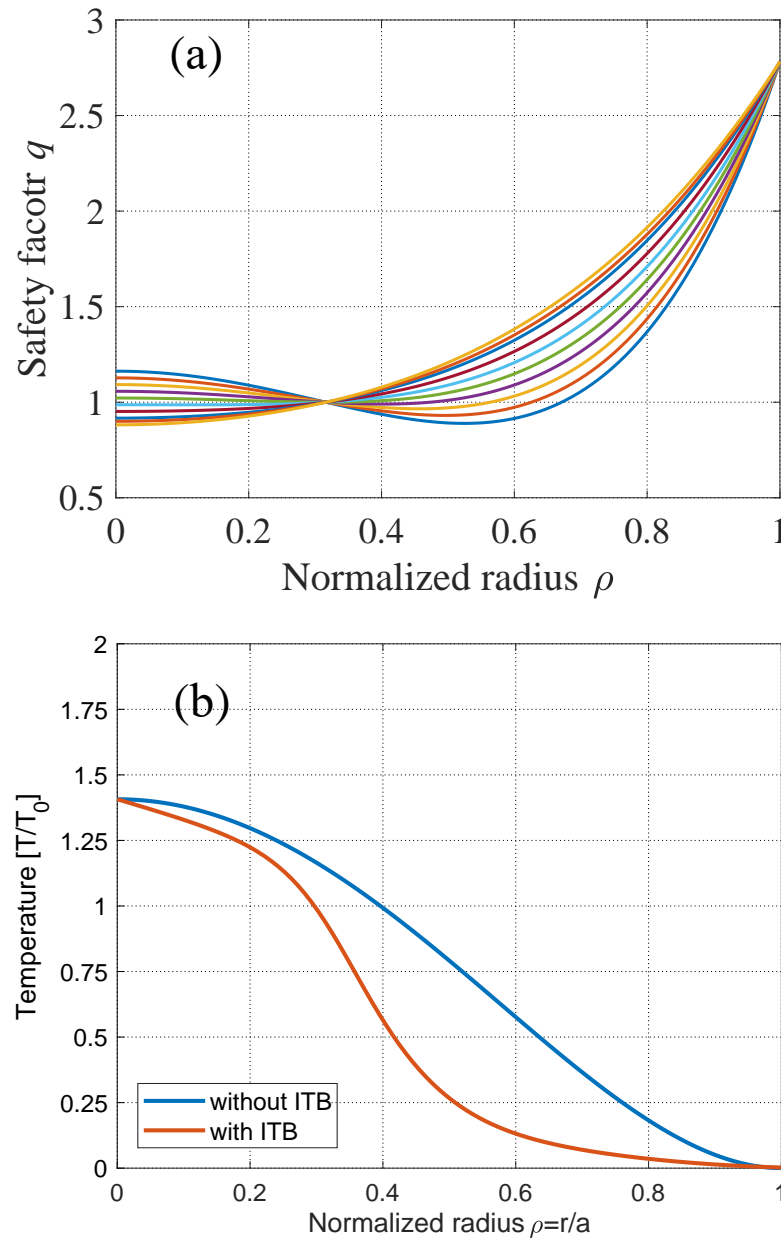


Figure 9. (a) q -profiles with various magnetic shear \hat{s} at $q = 1$ surface and (b) the pressure profile in absence (blue) and presence (orange) of an ITB.

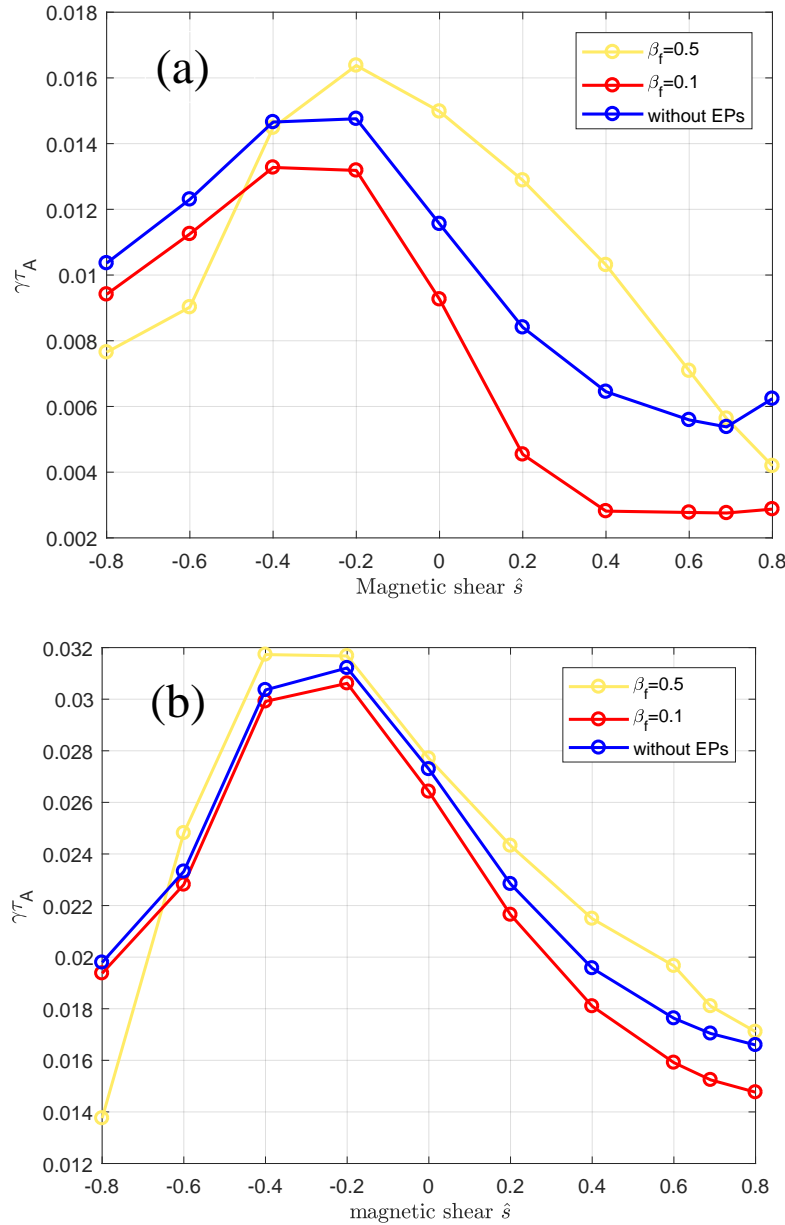


Figure 10. Normalized growth rates as functions of the magnetic shear \hat{s} at $q = 1$ surface in (a) absence and (b) presence of an ITB for various EP- β fractions β_f .

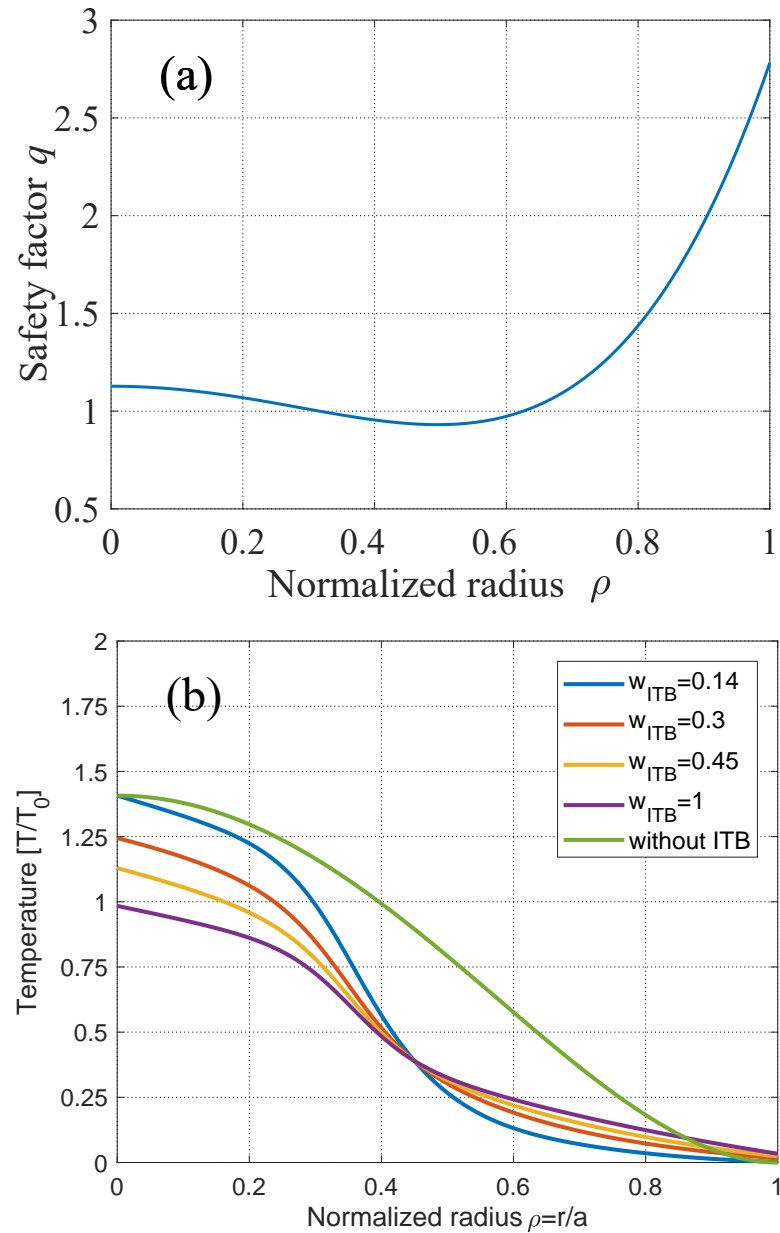


Figure 11. (a) q profile with $\hat{s} = -0.6$ at $q = 1$ surface, and (b) pressure profiles with various ITB widths.

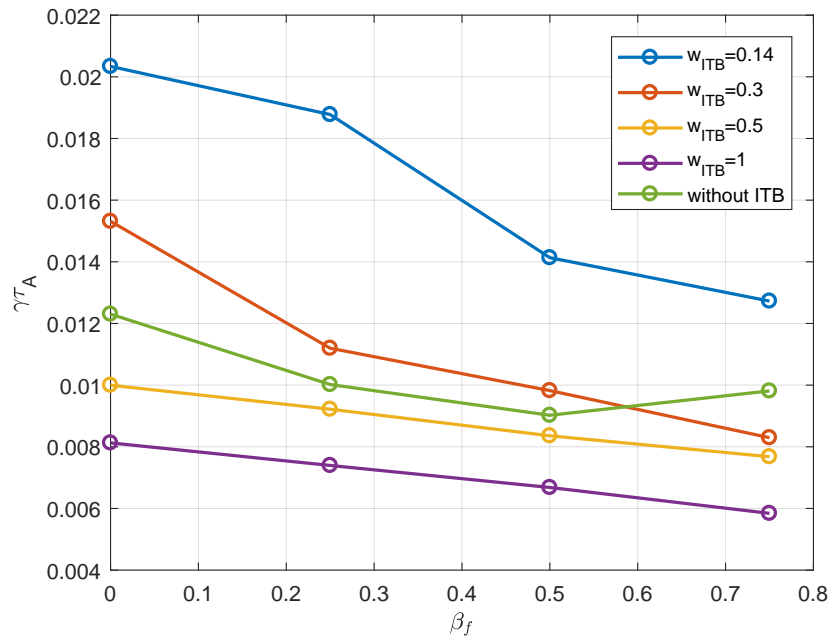


Figure 12. Normalized growth rates as functions of EP- β fraction β_f for various ITB widths.